Ultra-bright, efficient and stable perovskite light-emitting diodes

https://doi.org/10.1038/s41586-022-05304-w

Received: 19 August 2021

Accepted: 1 September 2022

Published online: 09 November 2022

Check for updates

Joo Sung Kim[1,9], Jung-Min Heo[1,9], Gyeong-Su Park[1,2,3], Seung-Je Woo[1], Changsoon Cho[4], Hyung Joong Yun[5], Dong-Hyeok Kim[1], Jinwoo Park[1], Seung-Chul Lee[6,7], Sang-Hwan Park[1], Eojin Yoon[1], Neil C. Greenham[4] & Tae-Woo Lee[1,2,7,8] ✉

Metal halide perovskites are attracting a lot of attention as next-generation light-emitting materials owing to their excellent emission properties, with narrow band emission[1–4]. However, perovskite light-emitting diodes (PeLEDs), irrespective of their material type (polycrystals or nanocrystals), have not realized high luminance, high efficiency and long lifetime simultaneously, as they are influenced by intrinsic limitations related to the trade-off of properties between charge transport and confinement in each type of perovskite material[5–8]. Here, we report an ultra-bright, efficient and stable PeLED made of core/shell perovskite nanocrystals with a size of approximately 10 nm, obtained using a simple in situ reaction of benzylphosphonic acid (BPA) additive with three-dimensional (3D) polycrystalline perovskite films, without separate synthesis processes. During the reaction, large 3D crystals are split into nanocrystals and the BPA surrounds the nanocrystals, achieving strong carrier confinement. The BPA shell passivates the undercoordinated lead atoms by forming covalent bonds, and thereby greatly reduces the trap density while maintaining good charge-transport properties for the 3D perovskites. We demonstrate simultaneously efficient, bright and stable PeLEDs that have a maximum brightness of approximately 470,000 cd m^{-2}, maximum external quantum efficiency of 28.9% (average = 25.2 ± 1.6% over 40 devices), maximum current efficiency of 151 cd A^{-1} and half-lifetime of 520 h at 1,000 cd m^{-2} (estimated half-lifetime >30,000 h at 100 cd m^{-2}). Our work sheds light on the possibility that PeLEDs can be commercialized in the future display industry.

Metal halide perovskites (MHPs) are being studied as promising candidates for light emitters because of their narrow emission spectra (full-width at half-maximum ≈ 20 nm), easy colour tuning, excellent charge-transport properties and low-cost solution processability[1–4]. Because of these advantages, research has mainly focused on achieving highly efficient operation of perovskite light-emitting diodes (PeLEDs). By introducing a perovskite nanocrystal (NC) structure colloidally synthesized with organic ligands or cation alloying (for example, $FA_xGA_{1-x}PbBr_3$), a high current efficiency of 108 cd A^{-1} and external quantum efficiency (EQE) of 23.4% have been achieved, by realizing strong carrier confinement and bulk/surface defect suppression[3,5–12]. However, in these perovskite nanocrystal (PeNC) emitters, the insulating characteristics of the organic ligands can impede charge injection and transport, and thereby limit the brightness and the operational lifetime despite their high luminous efficiency[8,13–15]. By contrast, three-dimensional (3D) polycrystalline perovskite (hereafter, 3D perovskite) film without such organic ligands has good charge-transport characteristics and simple fabrication processes (maximum luminance >100,000 cd m^{-2}, device half-lifetime (T_{50}) >200 h at initial brightness of 100 cd m^{-2}), but suffers from low luminous efficiency because of the poor charge confinement effect in the big grains of >100 nm, and non-radiative recombination defects at the grain boundary[16–20]. Although improvements in both perovskite nanocrystals and 3D perovskites have enabled far-reaching advances in the EQE of PeLEDs, owing to the inevitable trade-off between the charge confinement and charge transport, state-of-the-art efficient PeLEDs, with a maximum EQE > 20%, mostly suffer from low brightness (about 10,000 cd m^{-2})[7,10,15] and short T_{50} (<100 h at initial brightness of 100 cd m^{-2})[10]. Therefore, developing a perovskite material system that enables high brightness, high efficiency and long device lifetime simultaneously is of great importance at the current stage of research on PeLEDs.

Here, we developed a simple method to produce in situ-formed core/shell NCs (hereafter, in situ core/shell) by reacting 3D perovskite films with benzylphosphonic acid (BPA), which can split large crystals into PeNCs and surround them to form a PeNC@BPA composite, in which BPA exists as an organic shell material[21]. The significantly reduced particle size of in situ core/shell perovskites (10 ± 2 nm) compared with that of the 3D perovskites (205 ± 97 nm) showed significantly improved carrier confinement, and the phosphonate group of BPA

[1]Department of Materials Science and Engineering, Seoul National University, Seoul, Republic of Korea. [2]Research Institute of Advanced Materials, Seoul National University, Seoul, Republic of Korea. [3]Institute of Next-Generation Semiconductor Convergence Technology, Daegu Gyeongbuk Institute of Science and Technology (DGIST), Daegu, Republic of Korea. [4]Cavendish Laboratory, Department of Physics, University of Cambridge, Cambridge, UK. [5]Advanced Nano Research Group, Korea Basic Science Institute (KBSI), Daejeon, Republic of Korea. [6]PEROLED Co. Ltd., Seoul, Republic of Korea. [7]Soft Foundry, Seoul National University, Seoul, Republic of Korea. [8]School of Chemical and Biological Engineering, Institute of Engineering Research, Seoul National University, Seoul, Republic of Korea. [9]These authors contributed equally: Joo Sung Kim, Jung-Min Heo. ✉e-mail:twlees@snu.ac.kr

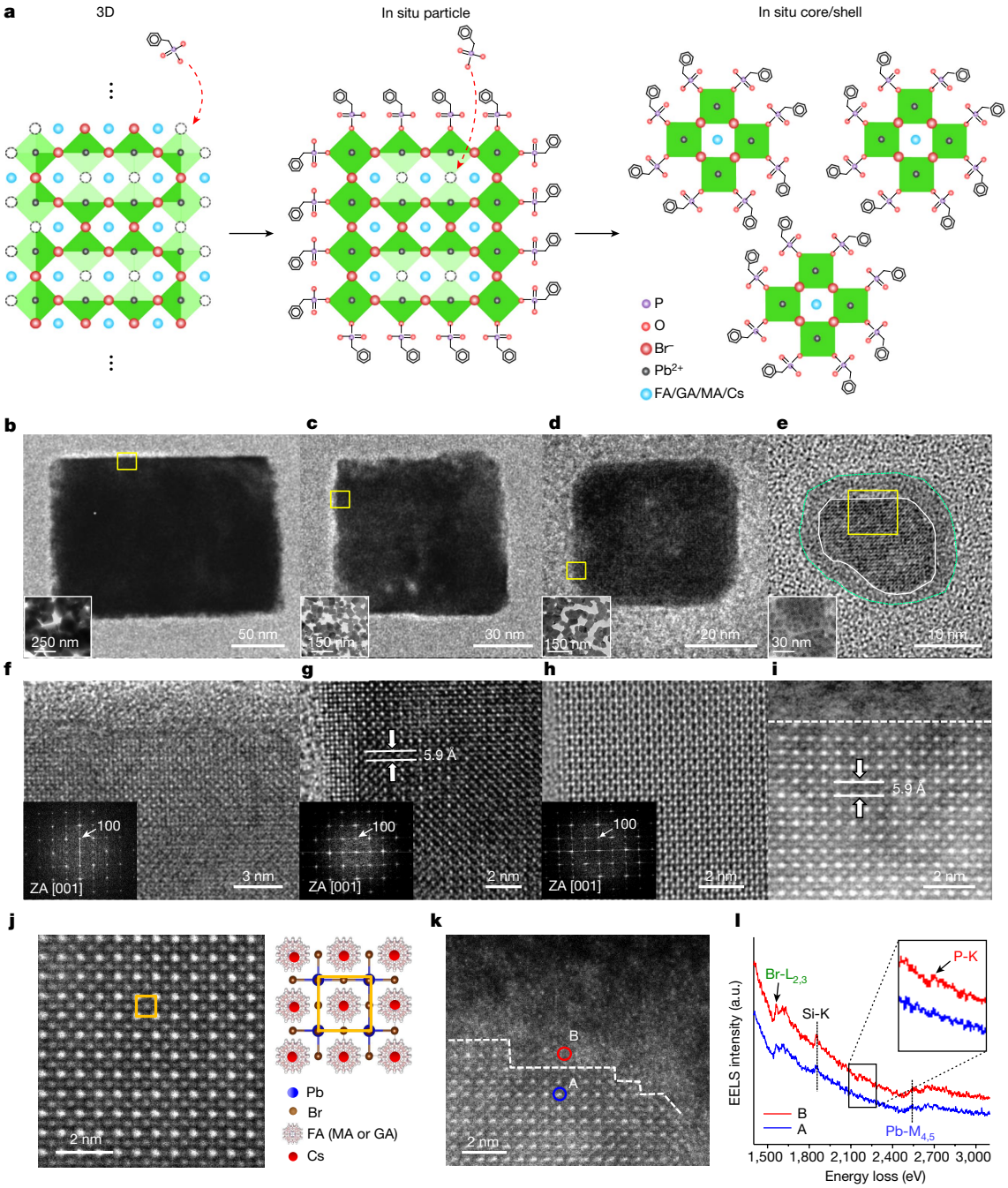

Fig. 1 | Emergence of in situ core/shell perovskite with BPA treatment. **a**, Schematic illustration of the transformation process of 3D (left) into in situ particle (middle) and in situ core/shell (right) structures by BPA treatment. FA, formamidinium; GA, guanidinium; MA, methylammonium. **b**–**e**, TEM images of perovskite nanograins during in situ core/shell synthesis with reaction times of 1 s (**b**), 10 s (**c**), 20 s (**d**) and 30 s (**e**). (Insets: low-magnification TEM images.) **f**–**h**, High-resolution TEM images of the boxed regions in **b**–**d**. (Insets: fast Fourier transform diffractograms showing the cubic lattice structure; ZA, zone axis). **i**, High-resolution HAADF-STEM image of the single in situ core/shell perovskite particle taken from the boxed region in **e**, showing a flat interface between the perovskite core and the BPA shell. **j**, Atomically resolved HAADF-STEM image of the core region taken from the in situ core/shell perovskite particle with atomic structure model, showing the perfect 3D perovskite crystal structure. **k**, High-resolution STEM image focusing on the surface region of in situ core/shell perovskite particle. **l**, The EEL spectra acquired from positions A and B highlighted in **k**. The Si peak is a background signal from the silicon nitride TEM window grid (a.u., arbitrary unit).

effectively passivated the defect sites by binding covalently to under-coordinated Pb^{2+}. In the in situ core/shell perovskites, the trap density was greatly decreased and the radiative recombination efficiency was significantly increased compared to the 3D perovskites. PeLEDs based on the in situ core/shell structure showed a maximum current efficiency of 151 cd A^{-1} (maximum EQE of 28.9%), maximum brightness of approximately 470,000 cd m^{-2}, very little efficiency roll-off (about 5% even at 400,000 cd m^{-2}) and half-lifetime of 520 h at an initial brightness of 1,000 cd m^{-2} (estimated half-lifetime >30,000 h at 100 cd m^{-2}) with green emission at the electroluminescence peak of 540 nm, and therefore shows excellent efficiency, luminance and lifetime simultaneously.

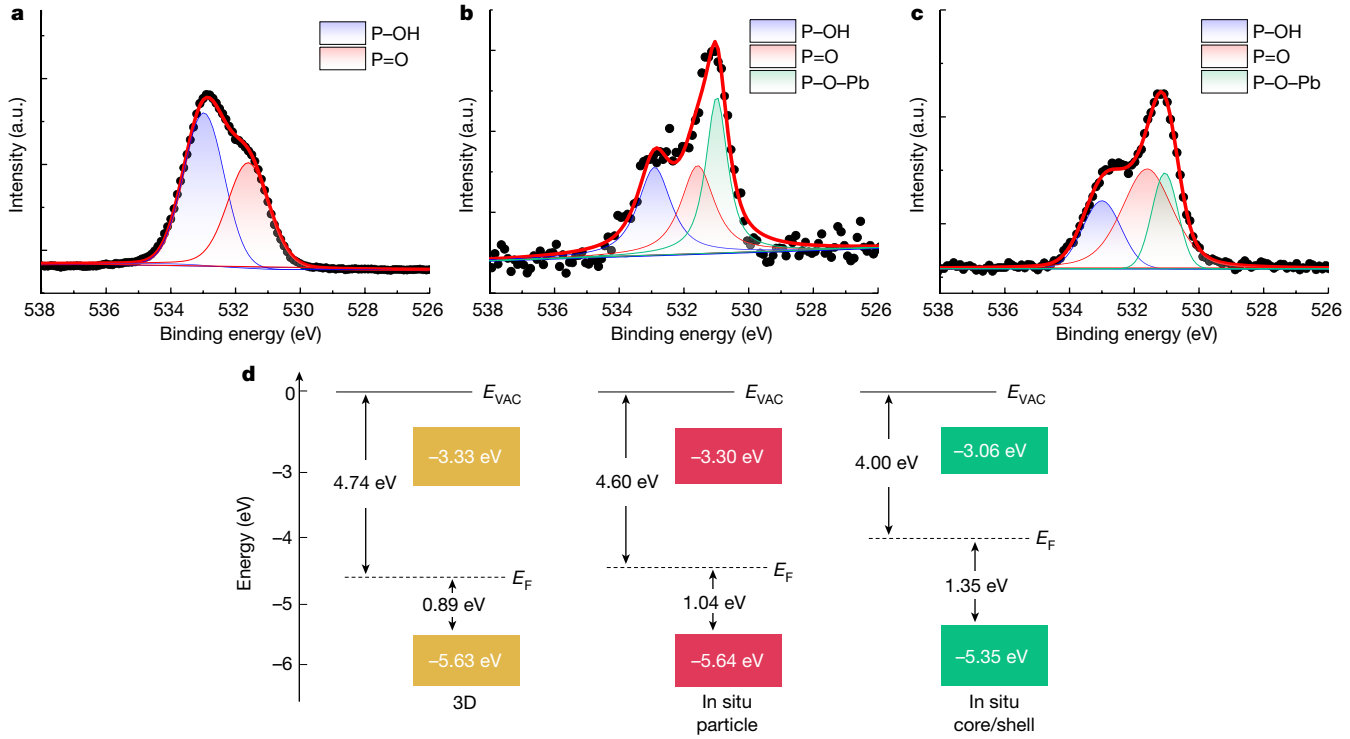

Fig. 2 | Surface passivation of BPA ligand. a–c, O 1*s* XPS core-level spectra of BPA (**a**), in situ particle perovskite (**b**) and in situ core/shell perovskite (**c**). **d**, Energy level diagram of the pristine 3D, in situ particle, in situ core/shell perovskites obtained from parameters derived from UPS spectra. (E_{VAC}, vacuum level; E_F, Fermi level).

In situ nanostructure formation by BPA treatment

We first show how posttreatment using BPA forms the in situ nanostructure of the perovskite crystal. 3D perovskite film of $(FA_{0.7}MA_{0.1}GA_{0.2})_{0.87}Cs_{0.13}PbBr_3$ was fabricated (Fig. 1a, left) using the additive-based nanocrystal pinning (A-NCP) method[3]. In this case, ionic defects with low formation energy exist on the crystal surface and inside the crystal, acting as a cause of ion migration and carrier trapping, thereby significantly reducing the luminescence efficiency and operational stability[19]. First, we added BPA as an additive into the precursor solution, implementing an in situ particle structure in which BPA covers the surface of crystals by attaching as a ligand to the undercoordinated Pb on the surface of 3D perovskites (Fig. 1a, centre). The surface of the 3D perovskite film initially had an irregular shape due to a defective surface; after addition of up to 10 mol% of BPA into the precursor, the fabricated film developed a very clear cubic structure as the BPA molecules assembled on the surface (Extended Data Fig. 1).

The perovskite thin film was further exposed to a BPA solution in tetrahydrofuran (THF), forming in situ core/shell perovskite (Fig. 1a, right). Unlike other long alkyl ligands (for example, oleic acid, decylamine and octylphosphonate), small BPA molecules with strong acidity can penetrate and intercalate into large perovskite crystals[22]. After sufficient time for the BPA to intercalate into the crystal, BPA binds to the surface sites within the crystal and splits the large crystal domain into a nanosized in situ core/shell structure that is surrounded by BPA.

The progressive particle refinement of large 3D perovskite grains (polycrystalline grains) to in situ core/shell perovskite (nanocrystal particle) was observed by high-resolution transmission electron microscopy (TEM). With increasing reaction time in BPA–THF solution, initially rectangular 3D crystals with a size of 200 nm showed gradual change in grain shape and decrease in grain size, and finally become spherical in situ core/shell structured nanograins with a size of 10 nm (Fig. 1b–i). The in situ core/shell synthesis process was further confirmed using atomic-scale scanning transmission electron microscopy (STEM) and scanning electron microscopy (SEM). At the beginning of the reaction, BPA molecules bind to defective surfaces of large crystals, which appear as dark contrast regions or vague boundaries on the STEM images, cracking the crystal out and thus reducing the grain size (Extended Data Fig. 2a–c). The grain splitting reveals new defective surfaces, the cycle of BPA binding and breakage is repeated and the grain size gradually decreases with increased coverage of a BPA shell on the surface (Extended Data Fig. 2d–g). Finally, when BPA molecules fully surround the 3D core, which then lacks a defective surface to which BPA can bind, the in situ core/shell structure is achieved (Fig. 1e,i). A perfect 3D lattice structure in the core part and a clear core/shell interface between perovskite and BPA molecule were identified by STEM image and electron energy loss spectra (EELS) (Fig. 1j–l and Extended Data Fig. 3). When the in situ core/shell synthesis was finished, these in situ core/shell grains were located adjacent to each other, after being aggregated by the excess BPA molecules around them, to form macroparticles, as observed in SEM and TEM images and energy dispersive spectroscopy (EDS) maps (Extended Data Figs. 4 and 5). The grain size distribution of these perovskite grains significantly decreased from the 3D perovskite (205 ± 97 nm) to the in situ particle structure (123 ± 34 nm) and further to the in situ core/shell structure (10 ± 2 nm) (Supplementary Data Fig. 1).

Surface passivation of the BPA shell

To elucidate the mode of binding between BPA and the perovskite structure, we performed X-ray photoelectron spectroscopy (XPS) and ultraviolet photoelectron spectroscopy (UPS) analysis. The existence of BPA in perovskite films can be confirmed by the emergence of new peaks in the P 2*p* and O 1*s* spectra only in the in situ particle and in situ core/shell perovskites (Supplementary Fig. 2a,b). The O 1*s* spectrum of the BPA before any reaction shows the main oxygen peak from the P–OH group at 533.0 eV and the P=O group at 531.5 eV in a ratio of 2:1, which is consistent with previously reported O 1*s* spectra of phosphonic acid

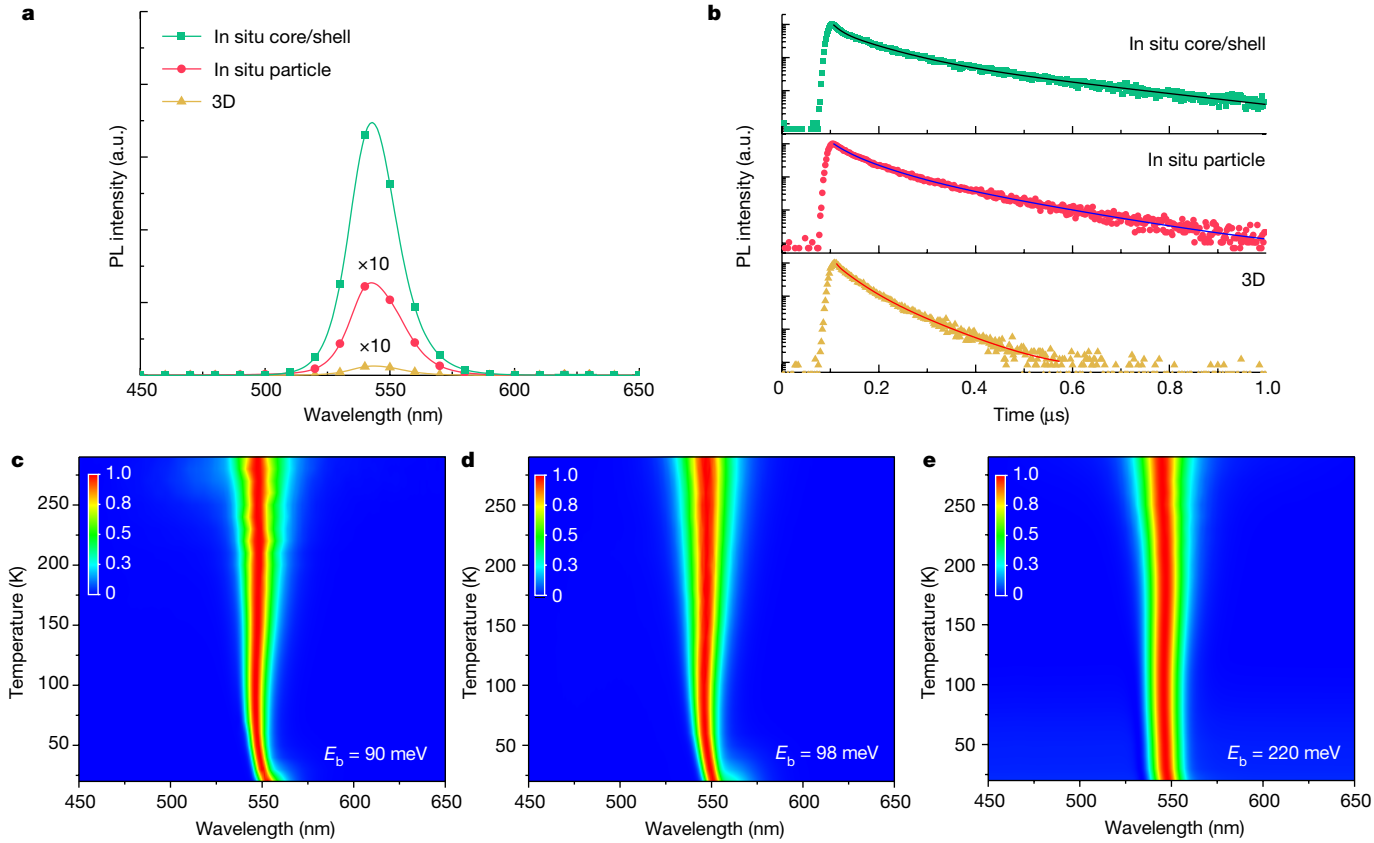

Fig. 3 | Luminescent property and defect passivation with BPA treatment. **a**,**b**, Steady-state PL spectra (**a**) and PL lifetime curves (**b**) of glass/BufHIL/perovskite thin films that used 3D, in situ particle and in situ core/shell structure. For comparison, PL intensity of 3D and in situ particle perovskites in **a** were magnified ten times. **c**–**e**, Two-dimensional (2D) map of temperature-dependent PL spectra of 3D (**c**), in situ particle (**d**) and in situ core/shell perovskite film (**e**) (normalized to peak value).

derivatives (Fig. 2a)[23,24]. By contrast, in the O 1*s* peak of in situ particles and in situ core/shell perovskites a new peak around 531.0 eV appeared (Fig. 2b,c). This change can be ascribed to the formation of covalent bonds during adsorption of phosphonate onto a metallic surface[23,25]; that is, BPA bonds to the surface of perovskites by forming a new Pb–O–P covalent bond and replaces the bromide vacancy site. In addition, the Pb 4*f* peak and the Br 3*d* peak of the BPA-induced structures are shifted to higher binding energy than in the 3D perovskite structure. This difference can be attributed to the higher electronegativity of oxygen atoms compared with that of bromines, and therefore modification of the Fermi level (Supplementary Fig. 2c,d). This was also confirmed by UPS analysis, which showed that the in situ particle and in situ core/shell perovskite have much lower work functions (4.6eV and 4.00eV, respectively) and higher energy offsets between the work function and valence band (Supplementary Fig. 3 and Fig. 2d). This difference can arise from the gradually diminishing self-p-doping effect caused by ionic defects at the surface and within the crystal in 3D perovskite and in situ particle perovskite, which was suppressed in the in situ core/shell perovskite.

Improvement in emission characteristics and defect passivation

We analysed the luminescence properties by conducting photoluminescence quantum efficiency (PLQE) analysis. Although perovskite thin films based on 3D and in situ particle structures showed comparably low internal quantum efficiencies (IQE) of 30% and 35%, respectively, in situ core/shell perovskite film showed a much higher IQE of 88% (Extended Data Fig. 6a–c). Steady-state photoluminescence (PL) spectra and time-correlated single photon counting (TCSPC) measurements also confirmed higher PL intensity and longer PL lifetimes in the in situ core/shell structure compared to the 3D and in situ particle perovskites (Fig. 3a,b). This great improvement in IQE can be realized by reducing the particle size to strengthen charge confinement and defect density by passivating defects, that is, undercoordinated Pb atoms and halide vacancies, which act as non-radiative recombination centres in the perovskite emitter. The improved charge confinement was confirmed by temperature-dependent PL analysis (Fig. 3c–e and Extended Data Fig. 6d–i). From 3D to in situ particle and in situ core/shell structures, the peak centre was blue-shifted, and the exciton binding energy (E_b) was increased from 90 meV to 220 meV; this change indicates that the in situ core/shell structure experiences a strong confinement effect from the grain size reduction.

To further confirm the passivation effect of the BPA-induced nanostructure, we performed trap-density analysis by fabricating a hole-only device and analysing the transport characteristics (Supplementary Fig. 4). The current–voltage (I–V) characteristics of these hole-only devices can be classified into three types of region, according to the slope (k): ohmic region ($k = 1$) in the low-injection regime, a trap-filled limited (TFL) region ($k > 3$)and a space-charge limited current (SCLC) regime ($k = 2$)[26]. In this way, the total trap state density inside the perovskite film can be calculated as follows:

$$n_t = 2\varepsilon\varepsilon_0 V_{TFL}/(eL^2)$$

where n_t is the trap state density, V_{TFL} is the trap-filled limit voltage, L is the thickness of the perovskites, e is the elementary charge, ε_0 and ε are the vacuum permittivity and relative permittivity, respectively. By

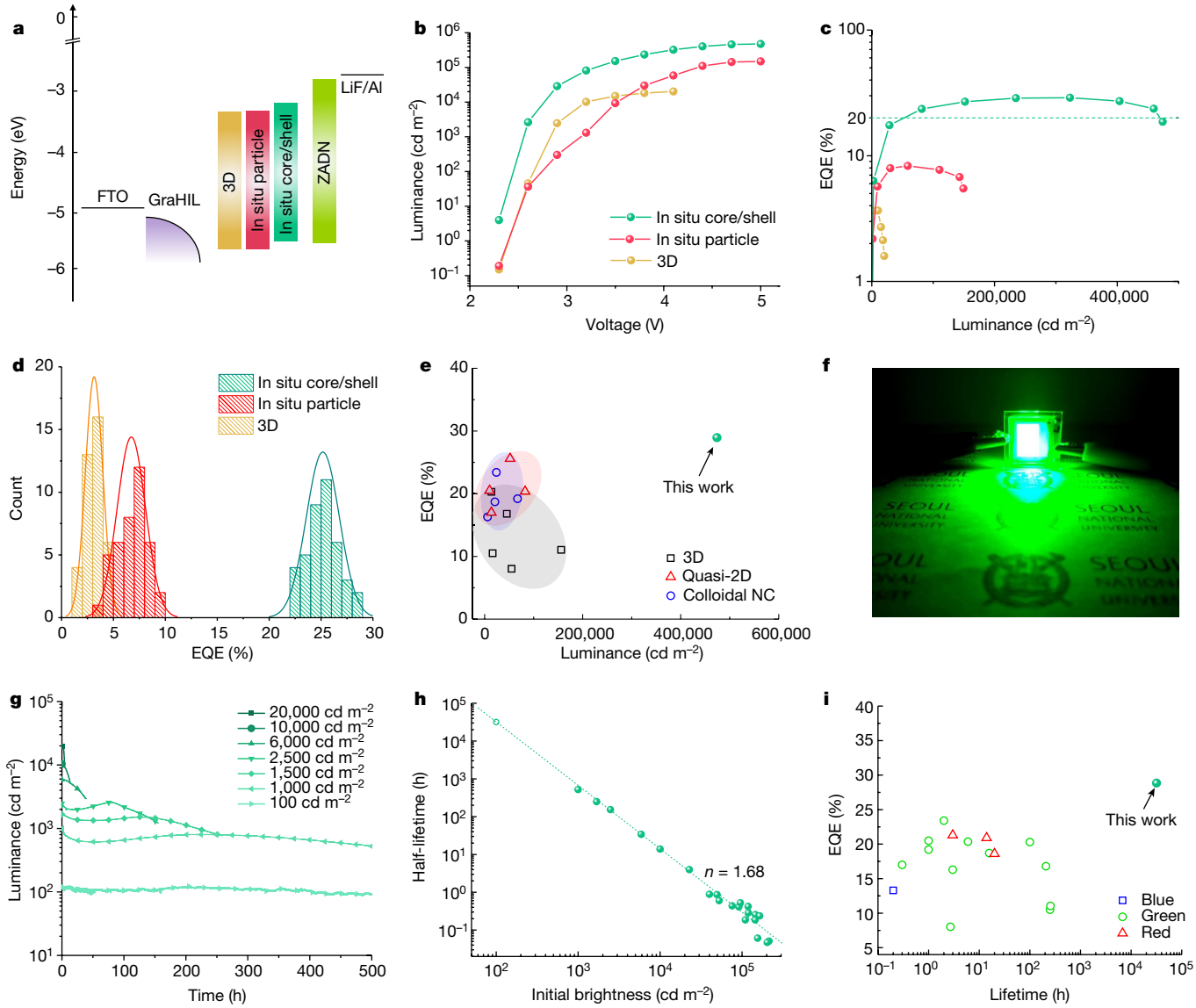

Fig. 4 | EL characteristics of PeLEDs with BPA treatment. a, Schematics of energy diagram of PeLEDs. **b**, Luminance versus voltage. **c**, EQE versus luminance. **d**, EQE histogram of PeLEDs (40 devices each). **e**, Summary of the reported green PeLEDs characteristics on the basis of maximum EQE and luminance. **f**, Photograph of operating large-area device (pixel size: 120 mm^2). **g**, Luminance versus time of PeLEDs on the basis of in situ core/shell perovskites at various initial brightness. **h**, Half-lifetime versus brightness from accelerated lifetime test of in situ core/shell PeLEDs. The open circle is the extrapolated half-lifetime for initial brightness of 100 cd m^{-2}. **i**, Summary of the reported PeLED characteristics on the basis of maximum EQE and estimated or measured half-lifetime at 100 cd m^{-2}.

estimating V_{TFL} as the intersection between the ohmic region and TFL region, we calculate $n_t = 3.50 \times 10^{16}$ cm^{-3} for 3D, $n_t = 2.36 \times 10^{16}$ cm^{-3} for in situ particle and $n_t = 1.37 \times 10^{16}$ cm^{-3} for in situ core/shell perovskites. This result is evidence that the passivation effect of the BPA-induced nanostructure in perovskite films also contributes to the increased luminescence efficiency. We also calculated the hole mobility (μ_h) of each device by applying the Mott–Gurney law equation in the Child region of trap-free SCLC transport, as below.

$$\mu_h = \frac{8L^3J}{9\varepsilon\varepsilon_0 V^2}$$

Here, J is the current density and V is the voltage. All devices had similar μ_h values: 3.26×10^{-2} cm^2 V^{-1} s^{-1} with 3D, 3.08×10^{-2} cm^2 V^{-1} s^{-1} with in situ particle and 2.99×10^{-2} cm^2 V^{-1} s^{-1} with in situ core/shell perovskites. This result indicates that the fast charge-transport property in 3D perovskites could be preserved in the in situ core/shell structure because excessive insulating ligand was not used.

Light-emitting diode performance

Encouraged by the simultaneously increased PL efficiency, decreased trap density and preserved fast charge transport, we fabricated LEDs based on the BPA-induced nanostructured perovskites (Fig. 4a and Supplementary Fig. 5). The PeLEDs based on in situ core/shell perovskites showed a maximum current efficiency of 151 cd A^{-1} and maximum EQE of 28.9%, calculated using the full angular electroluminescence distribution (Fig. 4b,c and Extended Data Fig. 7a–g)[27]. In contrast to many previously reported organic LEDs (OLEDs) and PeLEDs that have ultrathin emission layers (EMLs) (<50 nm), this is a remarkably high EQE, with an EML > 200 nm in devices in which the microcavity effects are diluted. The result emphasizes the important role of the photon recycling effect in thick EMLs[28–31]. Optical simulation verified that our PeLEDs can reach an EQE of 29.2% with the aid of the photon recycling effect (Supplementary Fig. 6). The detailed current–voltage–luminance characteristics are summarized in Extended Data Table 1. Also, the distribution of EQE and luminance obtained from 40 devices showed great

reproducibility (Fig. 4d and Extended Data Fig. 7h). In particular, to manufacture efficient in situ core/shell PeLEDs with great reproducibility, the crystallization process of the as-synthesized perovskite thin films must be controlled so that the grain size does not increase too much before the in situ reaction with BPA. When the A-NCP timing is not delayed and the processing temperature is kept at <18 °C, the grain size can be sufficiently small (<100 nm), so that BPA can completely penetrate the grains during the reaction, and thereby provide nanostructures that are favourable for obtaining high-efficiency devices (Extended Data Fig. 7i). The PeLEDs showed high maximum brightness of 473,990 cd m^{-2}, whereas 3D PeLEDs and in situ particle PeLEDs showed a maximum brightness of only 20,271 cd m^{-2} and 149,331 cd m^{-2}, respectively. The maximum brightness of in situ core/shell PeLEDs is the highest so far reported among PeLEDs based on any of the 3D, quasi-2D or colloidal NC structures, and is even comparable with the highest brightness of state-of-the-art inorganic quantum dot LEDs (334,000 cd m^{-2}) (Fig. 4e)[32]. Furthermore, owing to the fast charge transport with high IQE, we could realize an ultralow driving voltage of 2.7 V at a brightness of 10,000 cd m^{-2}, which is much lower than the driving voltage of any other state-of-the-art LEDs based on quasi-2D (4.7 V), PeNC (6 V) or organic $Ir(ppy)_2(acac)$ (4.8 V) structures (Supplementary Table 1). In situ core/shell PeLEDs also maintained an EQE value of ≥20% under ultra-high brightness conditions from 50,000 cd m^{-2} to 400,000 cd m^{-2}, and exhibited very low roll-off of about 5% at a luminance of 400,000 cd m^{-2} (Supplementary Table 2). These results are remarkable considering that reported high-efficiency nanocrystal PeLEDs with EQE > 20% have low brightness (approximately 10,000 cd m^{-2}) and large efficiency roll-off (>50% at >10,000 cd m^{-2}), because they use insulating ligands and therefore have a thickness of emitting layer that is mostly <30 nm, to compensate for the poor charge-transporting characteristics and to strengthen light outcoupling from the device (Fig. 4e). By contrast, these in situ core/shell perovskites are formed by in situ treatment of 3D perovskites without long insulating ligands, so both high efficiency and high brightness can be realized without significantly sacrificing charge transport, which in turn results in low-efficiency roll-off because of better charge balance with higher charge transport and thus no severe charge accumulation. We also fabricated bright large-area PeLEDs (pixel size: 120 mm^2) based on these in situ core/shell structures. These PeLEDs had high uniformity and maximum EQE of 22.5%; these results show the potential of hybrid perovskite emitters for use in solid-state lighting and display applications (Fig. 4f and Extended Data Fig. 8)[33].

Finally, the operational lifetimes of the PeLEDs were analysed by applying a constant current and monitoring the luminance. Compared with the T_{50} of 3D (0.2 h) and in situ particle (3.5 h) PeLEDs at initial brightness (L_0) = 10,000 cd m^{-2}, in situ core/shell PeLEDs showed a much longer T_{50} of 14 h, due to greatly improved luminescent efficiency without sacrifice of charge-transport properties (Extended Data Fig. 9). The operational lifetime of in situ core/shell PeLEDs was further measured at various L_0 from 1,000 cd m^{-2} to 200,000 cd m^{-2} (Fig. 4g–h). Specifically, in situ core/shell PeLEDs showed ultra-long T_{50} of 520 h at 1,000 cd m^{-2}. By using the accelerated lifetime equation ($L_0^n T_{50}$ = constant, where n is an acceleration factor)[34,35] with n = 1.68 over 21 devices, we estimated the T_{50} of the device at 100 cd m^{-2} to be 31,808 h, which is, to our knowledge, the highest T_{50} estimated so far in PeLEDs (Fig. 4h,i and Supplementary Table 3).

Conclusions

We demonstrated core/shell perovskite NCs with a size of approximately 10 nm by using the in situ reaction of BPA with 3D perovskite thin films. In the reaction process, BPA molecules penetrated into large 3D perovskite crystals and split them into nanosized crystals, thus surrounding the BPA with a core/shell structure. This in situ core/shell structure enabled increased carrier confinement, reduction in trap density and increase in luminous efficiency without sacrificing the charge-transport properties of 3D perovskites. As a result, simultaneously ultra-bright, efficient and stable PeLEDs with a maximum current efficiency of 151 cd A^{-1} (maximum EQE of 28.9%), maximum luminance of approximately 470,000 cd m^{-2}, very low-efficiency roll-off of about 5% at 400,000 cd m^{-2} and half-lifetime of 520 h at initial brightness of 1,000 cd m^{-2} (estimated half-lifetime >30,000 h at 100 cd m^{-2}) were demonstrated. These results suggest that PeLEDs are not only laboratory-level high-efficiency devices, but also promising candidates for commercial self-emissive displays and lighting applications that require ultra-high brightness and long operational lifetimes, comparable to those of state-of-the-art OLEDs or quantum dot LEDs.

Online content

Any methods, additional references, Nature Research reporting summaries, source data, extended data, supplementary information, acknowledgements, peer review information; details of author contributions and competing interests; and statements of data and code availability are available at https://doi.org/10.1038/s41586-022-05304-w.

1. Kim, Y.-H. et al. Multicolored organic/inorganic hybrid perovskite light-emitting diodes. *Adv. Mater.* **27**, 1248–1254 (2015).
2. Tan, Z.-K. et al. Bright light-emitting diodes based on organometal halide perovskite. *Nat. Nanotechnol.* **9**, 687–692 (2014).
3. Cho, H. et al. Overcoming the electroluminescence efficiency limitations of perovskite light-emitting diodes. *Science* **350**, 1222–1225 (2015).
4. Kim, Y.-H., Cho, H. & Lee, T.-W. Metal halide perovskite light emitters. *Proc. Natl Acad. Sci. USA* **113**, 11694–11702 (2016).
5. Yang, X. et al. Efficient green light-emitting diodes based on quasi-two-dimensional composition and phase engineered perovskite with surface passivation. *Nat. Commun.* **9**, 570 (2018).
6. Zhao, B. et al. High-efficiency perovskite–polymer bulk heterostructure light-emitting diodes. *Nat. Photonics* **12**, 783–789 (2018).
7. Kim, Y.-H. et al. Comprehensive defect suppression in perovskite nanocrystals for high-efficiency light-emitting diodes. *Nat. Photonics* **15**, 148–155 (2021).
8. Hassan, Y. et al. Ligand-engineered bandgap stability in mixed-halide perovskite LEDs. *Nature* **591**, 72–77 (2021).
9. Xiao, Z. et al. Efficient perovskite light-emitting diodes featuring nanometre-sized crystallites. *Nat. Photonics* **11**, 108–115 (2017).
10. Lin, K. et al. Perovskite light-emitting diodes with external quantum efficiency exceeding 20 per cent. *Nature* **562**, 245–248 (2018).
11. Kim, Y.-H., Kim, J. S. & Lee, T. Strategies to improve luminescence efficiency of metal-halide perovskites and light-emitting diodes. *Adv. Mater.* **31**, 1804595 (2019).
12. Park, M.-H. et al. Boosting efficiency in polycrystalline metal halide perovskite light-emitting diodes. *ACS Energy Lett.* **4**, 1134–1149 (2019).
13. Cho, H., Kim, Y.-H., Wolf, C., Lee, H.-D. & Lee, T.-W. Improving the stability of metal halide perovskite materials and light-emitting diodes. *Adv. Mater.* **30**, 1704587 (2018).
14. Liu, M., Matuhina, A., Zhang, H. & Vivo, P. Advances in the stability of halide perovskite nanocrystals. *Materials* **12**, 3733 (2019).
15. Dong, Y. et al. Bipolar-shell resurfacing for blue LEDs based on strongly confined perovskite quantum dots. *Nat. Nanotechnol.* **15**, 668–674 (2020).
16. Wehrenfennig, C., Eperon, G. E., Johnston, M. B., Snaith, H. J. & Herz, L. M. High charge carrier mobilities and lifetimes in organolead trihalide perovskites. *Adv. Mater.* **26**, 1584–1589 (2014).
17. Herz, L. M. Charge-carrier mobilities in metal halide perovskites: fundamental mechanisms and limits. *ACS Energy Lett.* **2**, 1539–1548 (2017).
18. Xu, W. et al. Rational molecular passivation for high-performance perovskite light-emitting diodes. *Nat. Photonics* **13**, 418–424 (2019).
19. Meggiolaro, D., Mosconi, E. & De Angelis, F. Formation of surface defects dominates ion migration in lead-halide perovskites. *ACS Energy Lett.* **4**, 779–785 (2019).
20. Zhang, L. et al. Suppressing ion migration enables stable perovskite light-emitting diodes with all-inorganic strategy. *Adv. Funct. Mater.* **30**, 2001834 (2020).
21. Ahmed, G. H., Yin, J., Bakr, O. M. & Mohammed, O. F. Successes and challenges of core/shell lead halide perovskite nanocrystals. *ACS Energy Lett.* **6**, 1340–1357 (2021).
22. Park, S. M., Abtahi, A., Boehm, A. M. & Graham, K. R. Surface ligands for methylammonium lead iodide films: surface coverage, energetics, and photovoltaic performance. *ACS Energy Lett.* **5**, 799–806 (2020).
23. Wagstaffe, M. et al. An experimental investigation of the adsorption of a phosphonic acid on the anatase TiO_2 (101) surface. *J. Phys. Chem. C* **120**, 1693–1700 (2016).
24. Li, F., Zhong, H., Zhao, G., Wang, S. & Liu, G. Adsorption of α-hydroxyoctyl phosphonic acid to ilmenite/water interface and its application in flotation. *Colloids Surfaces A Physicochem. Eng. Asp.* **490**, 67–73 (2016).
25. Xuan, T. et al. Highly stable $CsPbBr_3$ quantum dots coated with alkyl phosphate for white light-emitting diodes. *Nanoscale* **9**, 15286–15290 (2017).
26. Kim, H. et al. Proton-transfer-induced 3D/2D hybrid perovskites suppress ion migration and reduce luminance overshoot. *Nat. Commun.* **11**, 3378 (2020).
27. Jeong, S.-H. et al. Characterizing the efficiency of perovskite solar cells and light-emitting diodes. *Joule* **4**, 1206–1235 (2020).
28. Pazos-Outon, L. M. et al. Photon recycling in lead iodide perovskite solar cells. *Science* **351**, 1430–1433 (2016).

29. Stranks, S. D., Hoye, R. L. Z., Di, D., Friend, R. H. & Deschler, F. The physics of light emission in halide perovskite devices. *Adv. Mater.* **31**, 1803336 (2019).
30. Cho, C. et al. The role of photon recycling in perovskite light-emitting diodes. *Nat. Commun.* **11**, 611 (2020).
31. Cho, C. & Greenham, N. C. Computational study of dipole radiation in re-absorbing perovskite semiconductors for optoelectronics. *Adv. Sci.* **8**, 2003559 (2021).
32. Song, J. et al. Over 30% external quantum efficiency light-emitting diodes by engineering quantum dot-assisted energy level match for hole transport layer. *Adv. Funct. Mater.* **29**, 1808377 (2019).
33. Kim, Y.-H. et al. Exploiting the full advantages of colloidal perovskite nanocrystals for large-area efficient light-emitting diodes. *Nat. Nanotechnol.* **17**, 590–597 (2022).
34. Dai, X. et al. Solution-processed, high-performance light-emitting diodes based on quantum dots. *Nature* **515**, 96–99 (2014).
35. Woo, S.-J., Kim, J. S. & Lee, T.-W. Characterization of stability and challenges to improve lifetime in perovskite LEDs. *Nat. Photonics* **15**, 630–634 (2021).

Publisher's note Springer Nature remains neutral with regard to jurisdictional claims in published maps and institutional affiliations.

Springer Nature or its licensor (e.g. a society or other partner) holds exclusive rights to this article under a publishing agreement with the author(s) or other rightsholder(s); author self-archiving of the accepted manuscript version of this article is solely governed by the terms of such publishing agreement and applicable law.

© The Author(s), under exclusive licence to Springer Nature Limited 2022

Methods

Materials

Formamidinium bromide (FABr, >99.99%), methylammonium bromide (MABr, >99.99%) and guanidinium bromide (GABr, >99.99%) were purchased from Dyesol. Caesium bromide (CsBr), benzylphosphonic acid (BPA, >97%), tetrafluoroethylene-perfluoro-3,6-dioxa-4-methyl-7-octene-sulfonic acid copolymer (PFI), chlorobenzene (CB), tetrahydrofuran (THF), and molybdenum oxide (MoO_3) were purchased from Sigma-Aldrich. Lead bromide ($PbBr_2$>98.0% (T)) was purchased from TCI. 2,2′,2′′-(1,3,5-Benzinetriyl)-tris(1-phenyl-1*H*-benzimidazole) (TPBi) was purchased from OSM. 9,10-Di(naphthalene-2-yl)anthracen-2-yl-(4,1-phenylene)(1-phenyl-1*H*-benzo[d]imidazole) (ZADN) was purchased from Shinwon Chemtrade. Lithium fluoride (LiF) was supplied by Foosung. Unless otherwise stated, all materials were used without purification.

Preparation of MHP solution

The mixed-cation precursor ($(FA_{0.7}MA_{0.1}GA_{0.2})_{0.87}Cs_{0.13}PbBr_3$) was prepared by dissolving stoichiometric ratios of each of FABr, MABr, GABr, CsBr and $PbBr_2$ (molar ratio (FABr + MABr + GABr + CsBr) : $PbBr_2$ = 1.15:1) in DMSO at a concentration of 1.2 M (refs. [7,36]). In the case of the precursor solution for the in situ particle perovskite, 10 mol% of BPA relative to $PbBr_2$ was added. The solution was stirred overnight in an N_2-filled glovebox at room temperature before use.

Fabrication of PeLEDs

Prepatterned fluorine-doped tin oxide (FTO) (350 nm, 12–14 Ω sq^{-1}, 25 mm × 25 mm, Nippon Sheet Glass Co. Ltd.) glasses were sonicated in acetone and 2-propanol for 15 min each sequentially, then boiled in 2-propanol for 30 min. The surface of FTO substrates underwent ultraviolet-ozone treatment to achieve a hydrophilic surface. We used a previously described method to prepare a hole-injection layer (BufHIL) that had a gradient work function, by inducing vertical self-organization of PEDOT:PSS (CLEVIOS P VP AI4083) and PFI copolymer to have surface-enriched PFI buffer layer; the solution with 1:1 weight ratio of PEDOT:PSS to PFI was spin coated to form a 75 nm thickness, then annealed at 150 °C for 30 min (ref. [1]). After baking, the substrates were transferred to an N_2-filled glovebox for deposition of the MHP layer. MHP films with thicknesses of 270 nm were deposited by spin coating the precursor solution at 6,000 r.p.m. with the A-NCP process[3]: during the second spin step, TPBi-dissolved CB solution was dropped onto the spinning perovskite film. For synthesis of in situ core/shell perovskite film, BPA dissolved in THF solution was loaded on top of the perovskite, followed by a reaction time of 30 s and direct spin drying afterwards. Samples were then moved to the vacuum chamber (<10^{-7} Torr) to sequentially deposit ZADN (45 nm), LiF (1.2 nm) and Al (100 nm). The active area of 4.9 mm^2 was defined by shadow masking during deposition of the cathode. Finally, the fabricated PeLEDs were encapsulated in a glovebox under a controlled N_2 atmosphere (O_2 < 10.0 ppm, H_2O < 1.0 ppm) by using a glass lid and UV-curable epoxy resin with 15 min of UV (365 nm) treatment.

Perovskite film characterization

Images of the surfaces were obtained using a field-emission scanning electron microscope (SUPRA 55VP). XPS and UPS spectra were measured using a photoelectron spectrometer (AXIS-Ultra DLD, Kratos). A monochromatic AlKα line (1,486.6 eV) was used for XPS, and He I radiation (21.2 eV) was used for UPS. Steady-state photoluminescence spectra and ultraviolet–visible (UV–vis) absorption spectra were measured using a JASCO FP8500 spectrofluorometer and Lambda-465 UV–vis spectrophotometer. For transient PL decay measurements, a system composed of a streak camera (c10627, Hamamatsu) and a nitrogen pulse laser (337 nm, 20 Hz, Usho) was used. PLQY was measured with a PMT and monochromator (Acton Research Corporation) using a 325 nm He:Cd CW laser (Kimmon Koha) at the excitation power of 62.5 mW cm^{-2}. Direct and indirect emission from the perovskite film was measured to determine the accurate PLQY values. For the temperature-dependent PL measurements, the sample was mounted in a cryostat (Advanced Research Systems) under vacuum and the emission spectrum was analysed using a 405 nm laser diode (PicoQuant) at an excitation power of 34 μW cm^{-2}. For single-carrier device analysis, MoO_3 (30 nm) and Au (50 nm) were thermally deposited sequentially onto FTO/BufHIL/perovskite and encapsulated in an N_2 atmosphere to obtain the current–voltage curve using a Keithley 236 source measurement unit.

TEM characterizations

Perovskite thin films were deposited on a 5 nm thick silicon nitride membrane using the same spin-coating conditions as for the actual device. The membrane, with a size of 100 μm × 1,500 μm, was supported on a 100 μm thick silicon frame. The silicon nitride membrane grid was loaded on a sample holder for TEM characterization without further processing of the TEM sample preparation. Double Cs-corrected (S) TEM systems (Themis Z, ThermoFisher Scientific) equipped with EELS (Quantum ER965, Gatan) and EDS (Super-X EDS system) were used for atomic-scale structure imaging and chemical analysis of the samples at an accelerating voltage of 200 kV. Due to the electron beam damage of core/shell perovskite nanocrystals by high-energy electron illumination in TEM, we acquired high-resolution TEM images, high-resolution high-angle annular dark field (HAADF)-STEM images, and EELS and EDS data at the low dose rates. Core-loss EELS using a 2 Å nominal probe size and 1.8–2.0 eV energy resolution were obtained with exposures of 12 s (integrated by 60 scans with each taking for 0.2 s). EELS entrance aperture of 5 mm, and an energy dispersion of 0.5 eV ch^{-1} and 1.0 eV ch^{-1} were used for high-loss EELS (>1,500 eV).

Characterization of efficiency of PeLEDs

Electroluminescence efficiencies of the fabricated PeLEDs were measured using a Keithley 236 source measurement unit and a Minolta CS-2000 spectroradiometer. EQE of PeLEDs was calculated by measuring full angular electroluminescence distribution[27]. We cross-checked the accuracy of the analysis by conducting an independent analysis at the University of Cambridge with the same devices, from which we confirmed consistent results (Supplementary Fig. 7).

Lifetime analysis of PeLEDs

Operational lifetime of PeLEDs was measured under constant-current conditions by simultaneously tracking brightness and applied voltage using an M760 Lifetime Analyzer (McScience) with a control computer under an air-conditioned environment below 18 °C.

Optical simulation

Outcoupling efficiency, perovskite reabsorption A_{act} and parasitic absorption A_{para} were obtained from the calculated Poynting vectors at each interface of glass (n = 1.5, incoherent)/FTO (n = 1.9, 350 nm)/BufHIL (n = 1.5, 75 nm)/perovskite/ZADN (n = 2, 45 nm)/LiF (n = 1.4, 1.2 nm)/Al (n from ref. [37]), by using a recently proposed method[30,31] (n is refractive index). The imaginary part of the refractive index spectrum of perovskite was obtained from the measured absorbance, whereas the real part was assumed to be constant (n_{perov} = 2.3). The internal radiation spectrum was obtained by the reverse calculation from the measured external radiation spectrum. The maximum EQE values with photon recycling effect were obtained at each perovskite thickness, by integrating the results for dipoles with various wavelengths, orientations (vertical and horizontal), polarizations (s and p) and positions (20 positions uniformly distributed over the perovskite layer). The relationship between external and internal PLQE was calculated in the same way for the structure of glass/perovskite.

Data availability

The data that support the findings of this study are available from the corresponding authors upon reasonable request.

36. Cho, H. et al. High-efficiency polycrystalline perovskite light-emitting diodes based on mixed cations. *ACS Nano* **12**, 2883–2892 (2018).
37. Palik, E. D. & Ghosh, G. *Handbook of Optical Constants of Solids* (Academic Press, 1998).

Acknowledgements This work was supported by the National Research Foundation of Korea (NRF) grant funded by the Korea government (Ministry of Science, ICT and Future Planning) (NRF-2016R1A3B1908431). G.-S.P was supported by the DGIST R&D Program (22-CoE-NT-02) by the Korea government (Ministry of Education and Ministry of Science, ICT and Future Planning).

Author contributions J.S.K., J.-M.H. and T.-W.L. initiated and designed the study. J.S.K. and J.-M.H. fabricated LED devices and analysed data. G.-S.P. performed the TEM measurements. H.J.Y. conducted the UPS and XPS analysis. S.-J.W. and D.-H.K. conducted the temperature-dependent PL and photoluminescence quantum efficiency analysis. S.-J.W. and C.C. conducted the optical simulation of the devices with guidance from N.C.G. J.P. assisted with analysis of the TCSPC data. S.-C.L. provided support for characterization of the materials. S.-H.P. and E.Y. assisted with the fabrication of LED devices. T.-W.L. supervised the work. J.S.K. drafted the first version of the manuscript, with assistance from J.-M.H. and T.-W.L. All authors discussed the results and commented on the manuscript.

Competing interests The authors declare no competing interests.

Additional information

Supplementary information The online version contains supplementary material available at https://doi.org/10.1038/s41586-022-05304-w.

Correspondence and requests for materials should be addressed to Joo Sung Kim or Tae-Woo Lee.

Peer review information *Nature* thanks Lina Quan, Zhanhua Wei and the other, anonymous, reviewer(s) for their contribution to the peer review of this work.

Reprints and permissions information is available at http://www.nature.com/reprints.

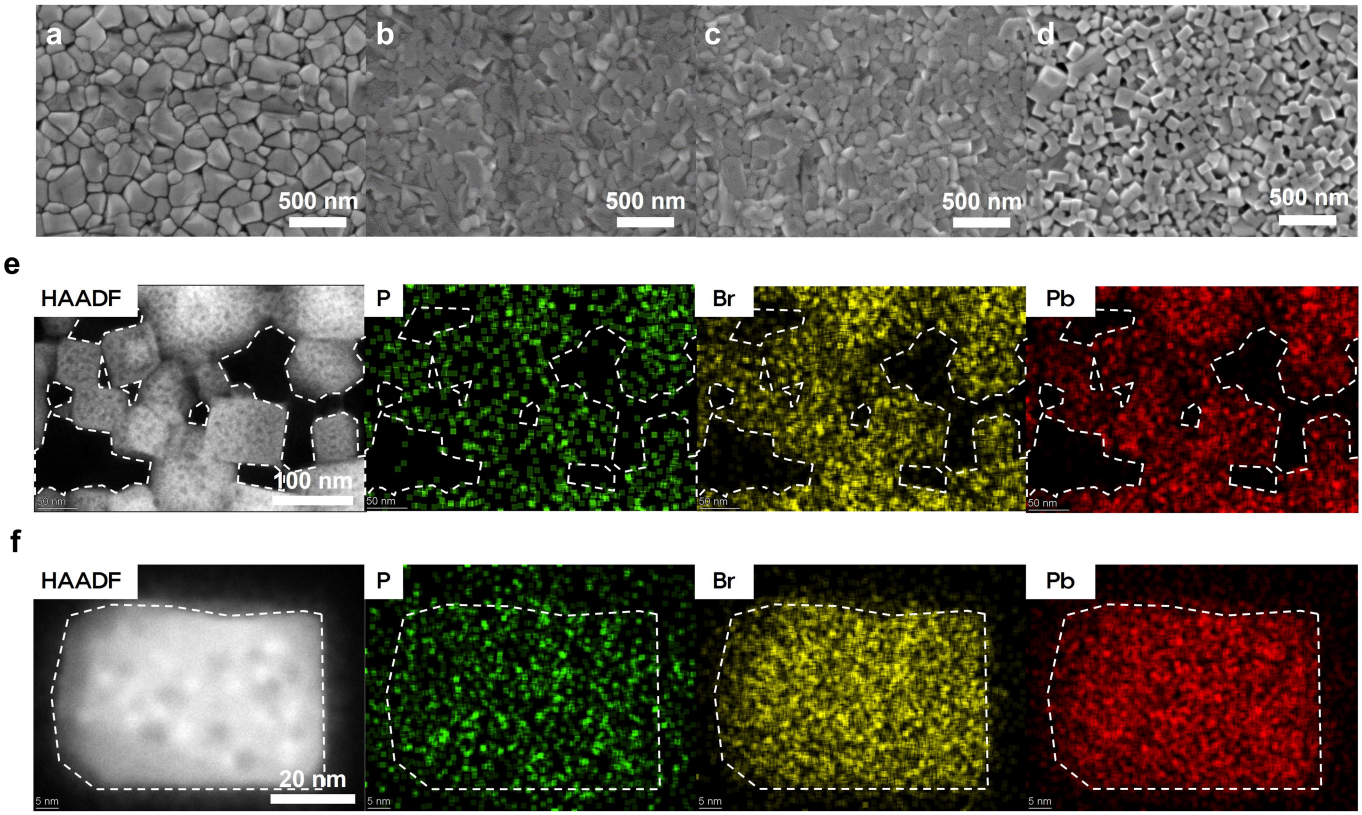

Extended Data Fig. 1 | Morphology of in situ particle perovskite thin films. SEM images of perovskite thin films made of 1.2M precursor solution with **a**, 0% (3D), **b**, 2.5%, **c**, 5%, **d**, 10% (in situ particle) molar ratio of BPA molecule relative to $PbBr_2$. **e**, HAADF-STEM image and EDS elemental maps of P (green), Br (yellow), and Pb (red), respectively. **f**, HAADF-STEM image and EDS elemental maps of a single perovskite grain showing the uniform dispersion of P (green), Br (yellow), and Pb (red) on the grain.

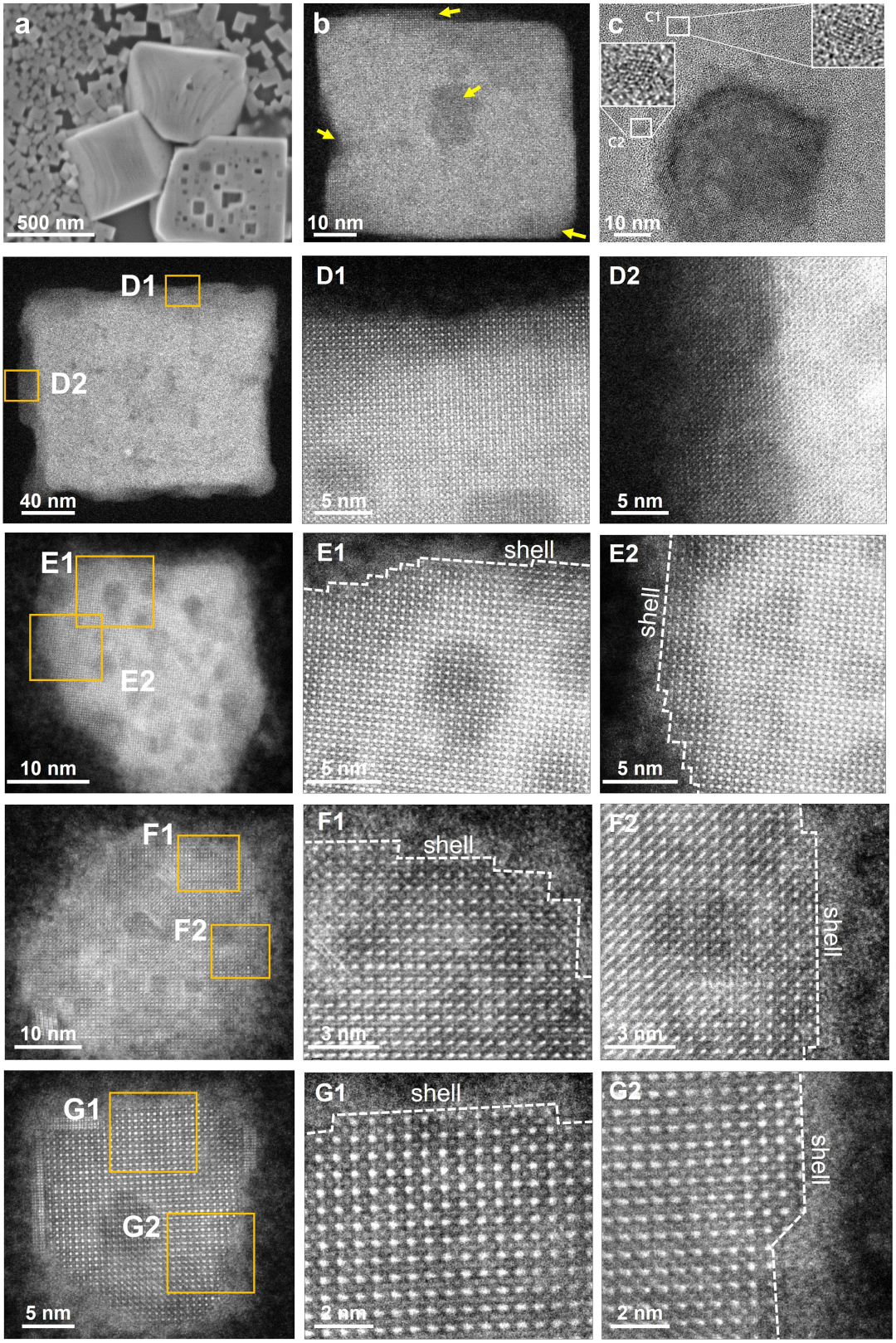

Extended Data Fig. 2 | Morphological characterization during in situ core/shell particle synthesis process. a, SEM image of a perovskite thin film (after 1s of reaction time with BPA-THF solution) showing small grains cracked out from large 3D grain. **b**, STEM image of 50 nm-size perovskite crystal during in situ core/shell synthesis process. Yellow arrows indicate the defective perovskite surfaces that can be bound with BPA. **c**, HR-TEM image of another perovskite crystal showing ultra-small nanocrystals segregated during in situ core/shell synthesis process. Insets: Magnified HR-TEM images of ultra-small nanocrystals taken from the white-boxed regions labelled C1 and C2. **d**, **e**, High-resolution HAADF-STEM images of single perovskite nanograins with decreasing grain size. Magnified HAADF-STEM images of the grain surfaces (D1, D2, E1, E2, F1, F2, G1, G2) demonstrate that the BPA shell coverages on the grain surfaces gradually increase and the defective surface regions decrease as the grain size decreases.

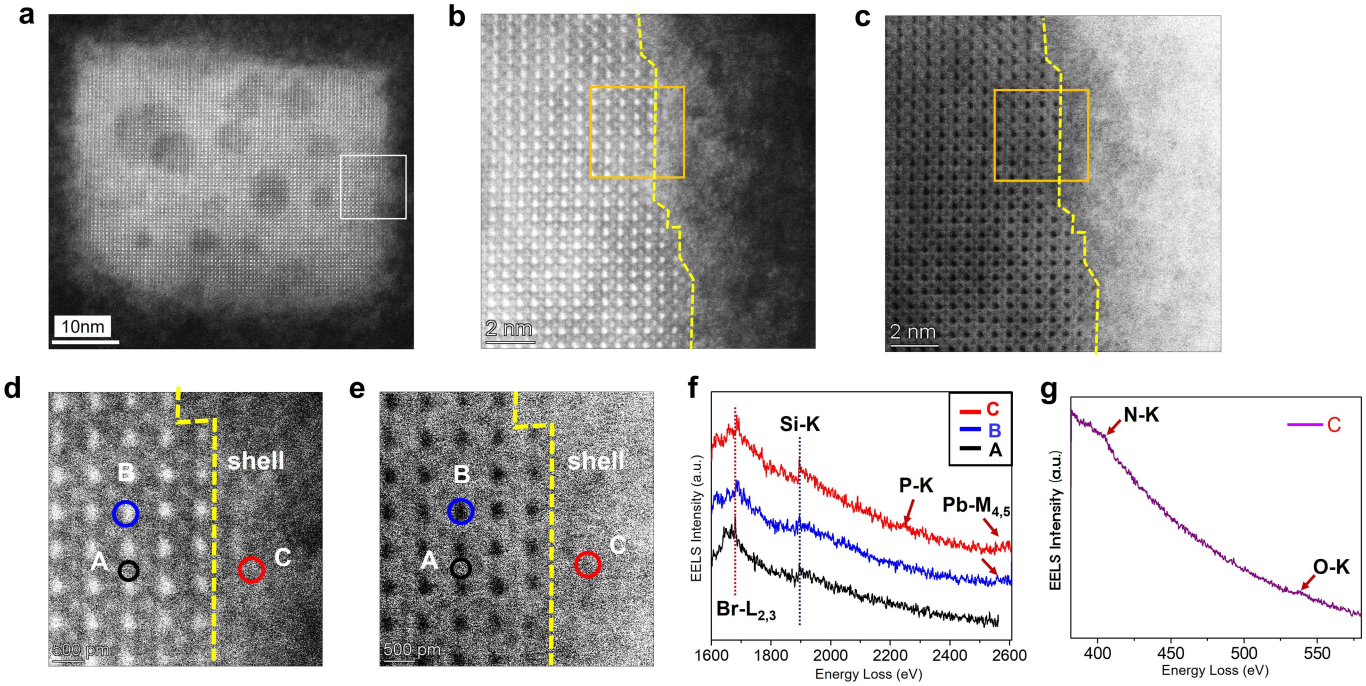

Extended Data Fig. 3 | Characterization of perovskite/BPA core/shell interface. a, High-resolution HAADF-STEM image of single perovskite grain formed during in situ core/shell synthesis process. **b**, **c**, Atomic-scale HAADF-STEM (**b**) and ABF-STEM (**c**) images of the boxed area denoted in **a**. **d**,**e**, Magnified HAADF-STEM (**d**) and ABF-STEM (**e**) images of the boxed area shown in **b** and **c** to indicate the positions of EELS acquisition. **f**, EEL spectra acquired at the atomic positions labelled A, B, and C in **d**, **e**. **g**, EEL spectrum in the energy-loss range of the N-K and O-K edges acquired at the position labelled C. The O-K peak indicates the presence of BPA shells, but N-K peak is simply a background signal from the silicon nitride TEM window grid.

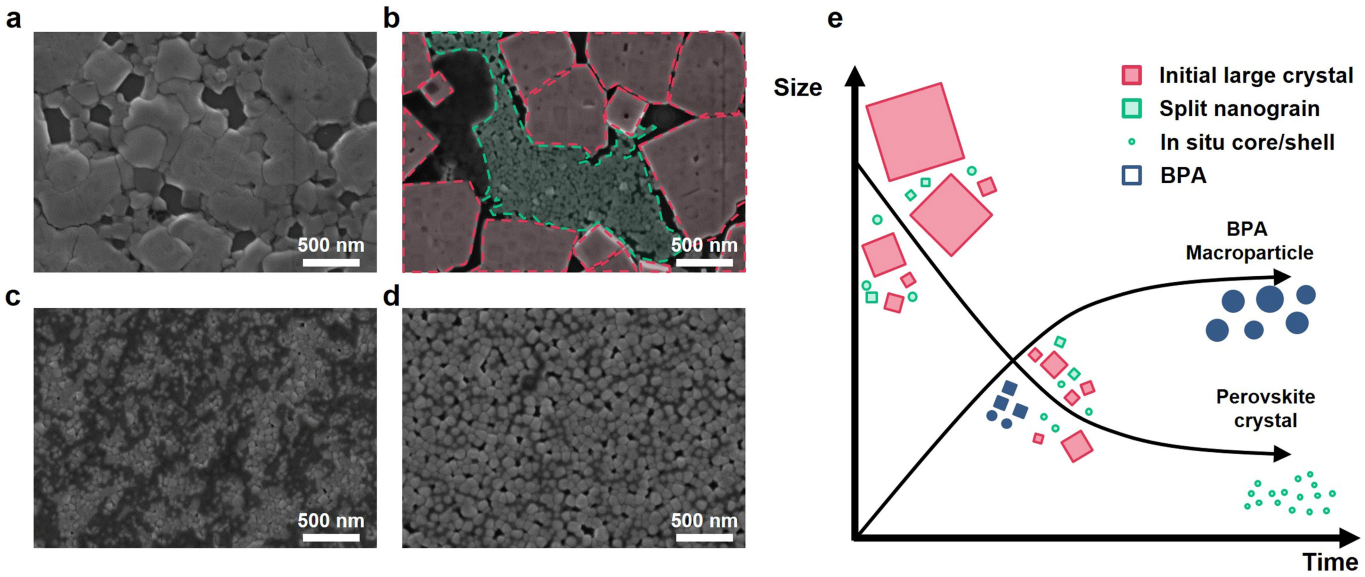

Extended Data Fig. 4 | SEM image of low-concentration (0.6 M) perovskite thin films with different reaction time between BPA solution and perovskite thin film. a, 3D perovskites without reaction, **b**, 1 s, **c**, 15 s, **d**, 30 s of exposure time to BPA-THF solution before spin-drying. Coloured regions indicate initial large crystals (red) and split nanograins (green). **e**, Schematic illustration of the growth process of BPA macroparticle domain and perovskite crystal forming in situ core/shell structure.

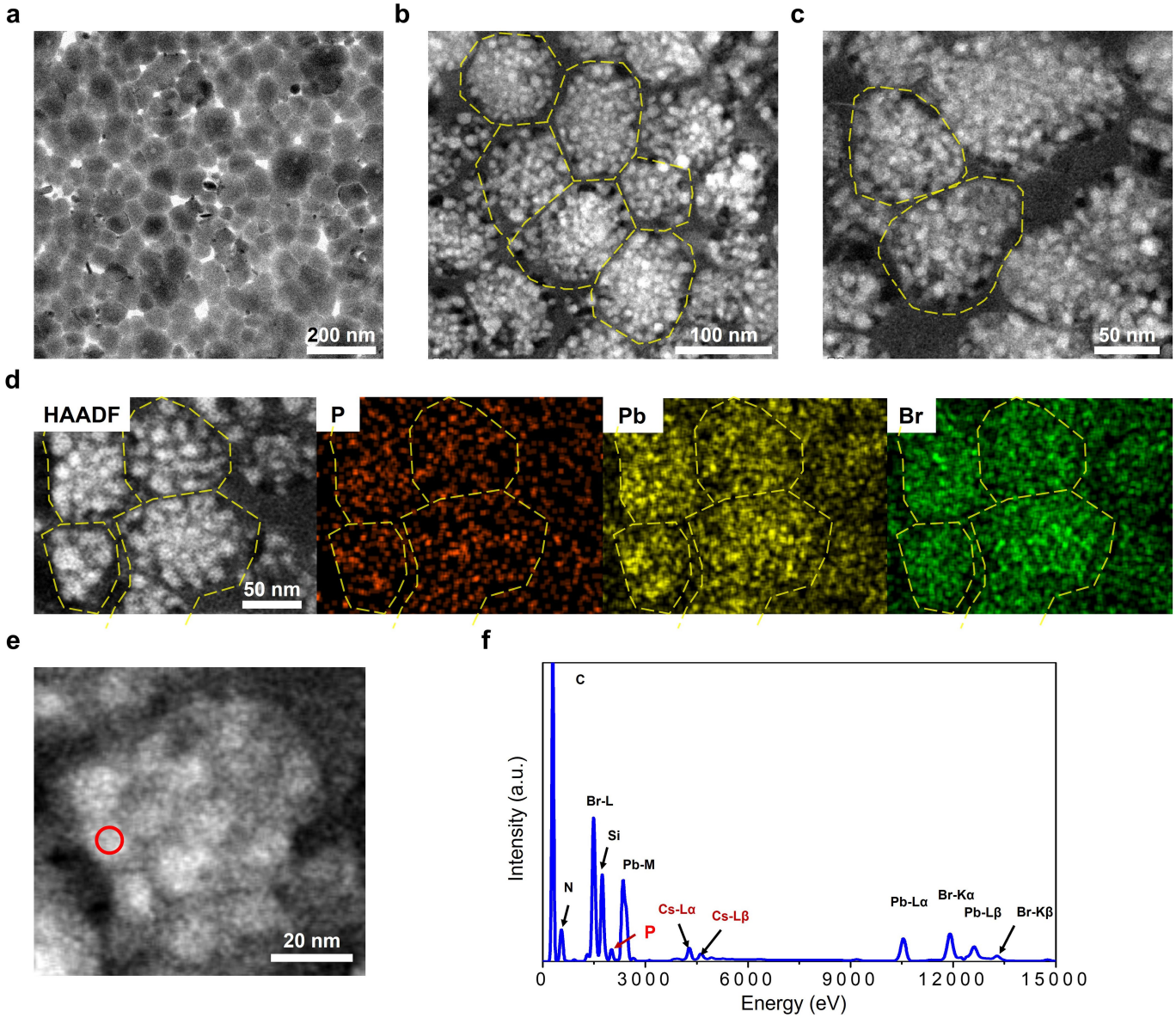

Extended Data Fig. 5 | HAADF-STEM analysis of in situ core/shell perovskites. a, TEM image and **b**, **c**, magnified HAADF-STEM images of in situ core/shell perovskite thin films. **d**, HAADF-STEM image of in situ core/shell grains and EDS elemental maps of P (red), Pb (yellow), and Br (green), respectively. The EDS maps clearly show the uniform dispersion of P (red) over macrograins. **e**, HAADF-STEM image of single macrograins consists of in situ core/shell nanoparticles. **f**, EDS spectrum acquired at the location of the red circled region in **e**.

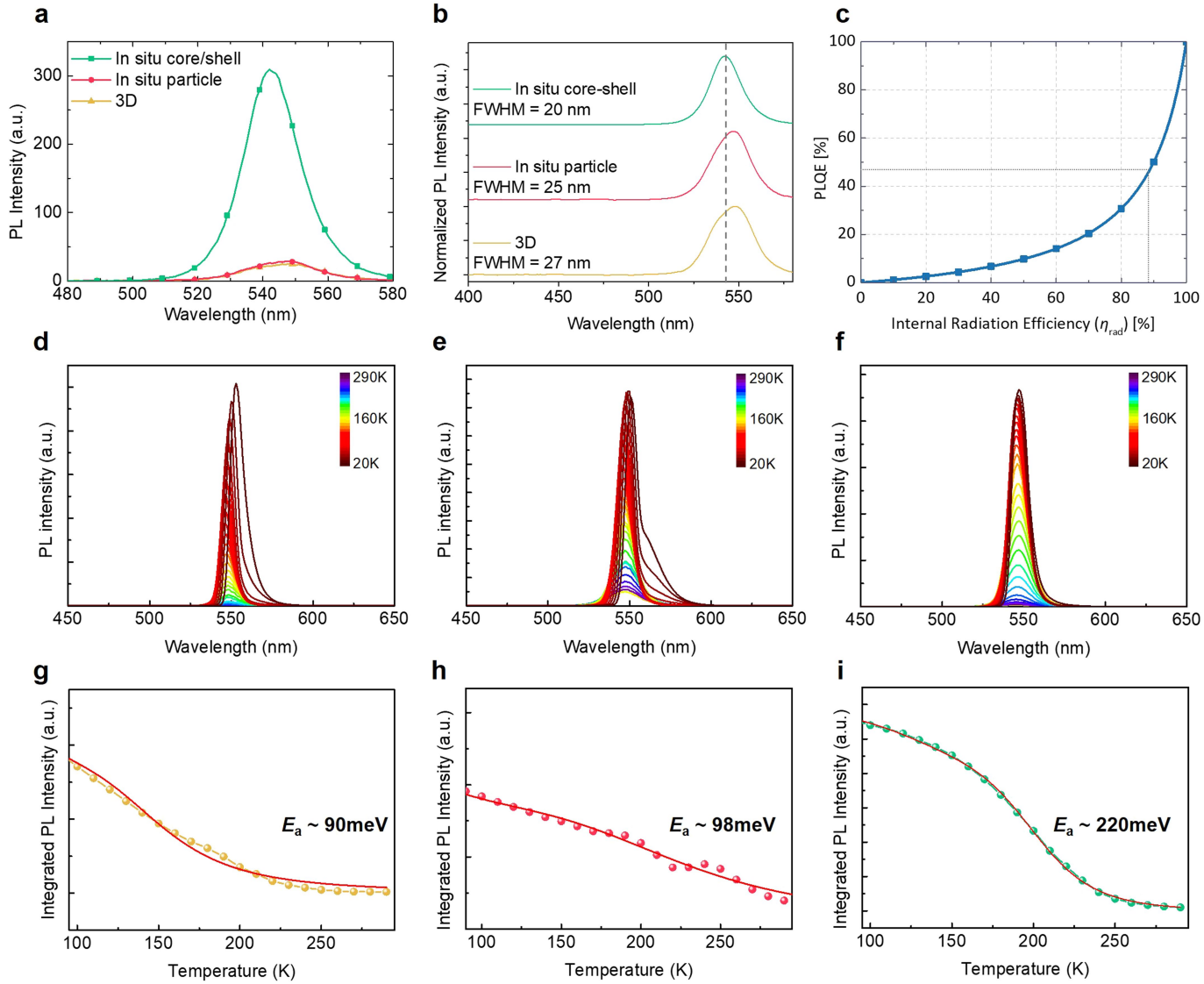

Extended Data Fig. 6 | Photoluminescence characteristics of perovskite thin films. a, PL spectra and **b**, normalized PL spectra of quartz/perovskite thin film measured in integrating sphere. **c**, External PLQE versus internal radiation efficiency (η_{rad}) (i.e. internal quantum efficiency, IQE) of perovskite film calculated considering the influence of perovskite reabsorption[30,31]. The external PLQE of the in situ core/shell structure was 46%, which corresponds to an IQE of 88%. **d**–**i**, Temperature-dependent PL spectrum and corresponding integrated PL intensity with calculated activation energy for: **d**,**g**, 3D, **e**,**h**, in situ particle, **f**,**i**, in situ core-shell perovskite thin films.

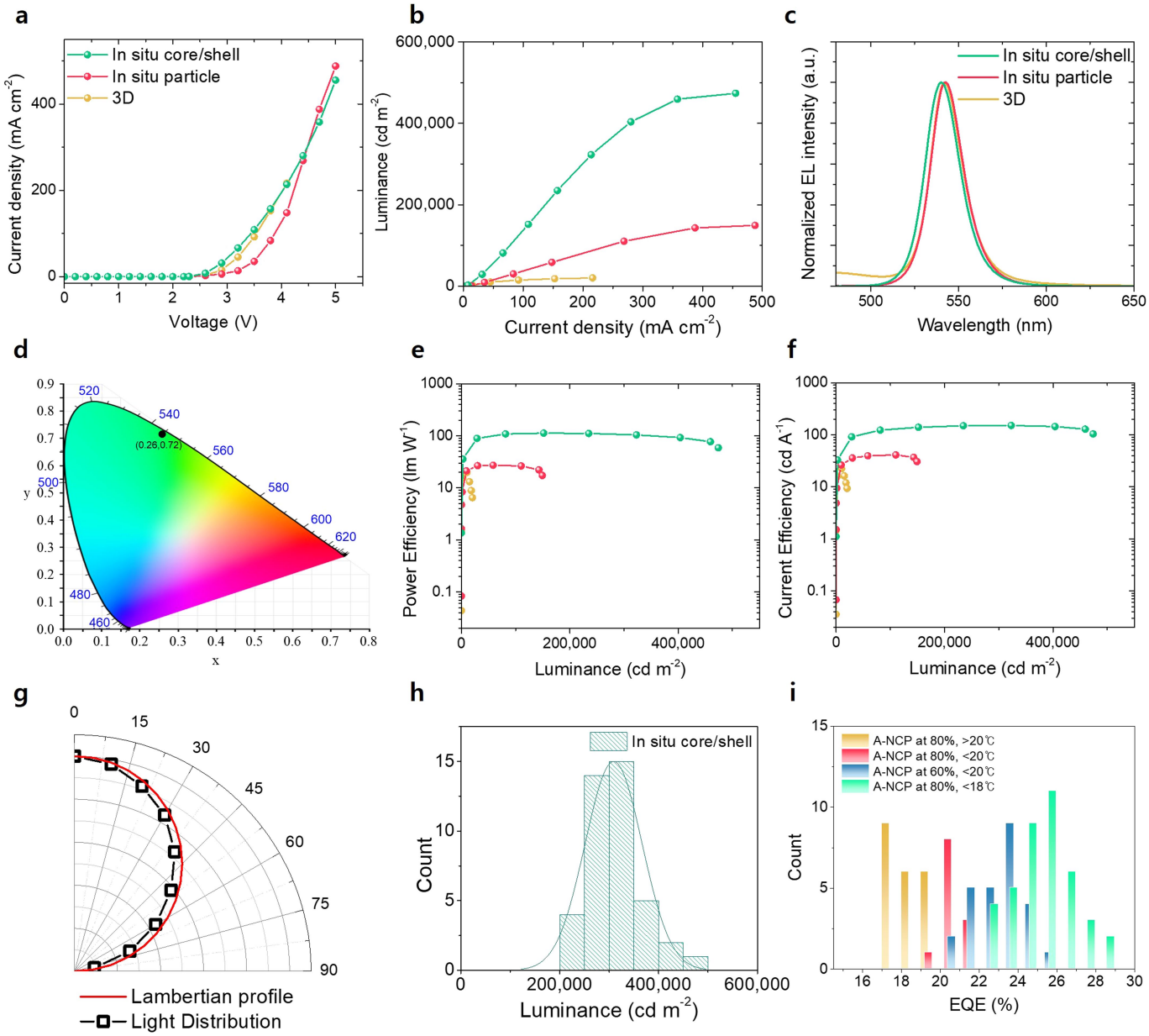

Extended Data Fig. 7 | Current-voltage-luminance characteristics of PeLEDs. a, Current density versus voltage; **b**, luminance versus current density; **c**, normalized EL spectra; **d**, CIE coordinate of in situ core/shell PeLEDs; **e**, power efficiency versus luminance; **f**, current efficiency versus luminance of PeLEDs based on 3D, in situ particle, in situ core/shell structure. **g**, Angle-dependent EL intensity and **h**, luminance histogram of PeLEDs based on in situ core/shell structure. **i**, EQE histogram of the PeLEDs based on in situ core/shell structure with different processing condition. As the temperature of the glove box increases or the A-NCP process is delayed, the grain size of the spin-coated perovskite thin film increases, which slows the penetration of the BPA solution into perovskite crystal and prevents full conversion of them into the in situ core/shell structure.

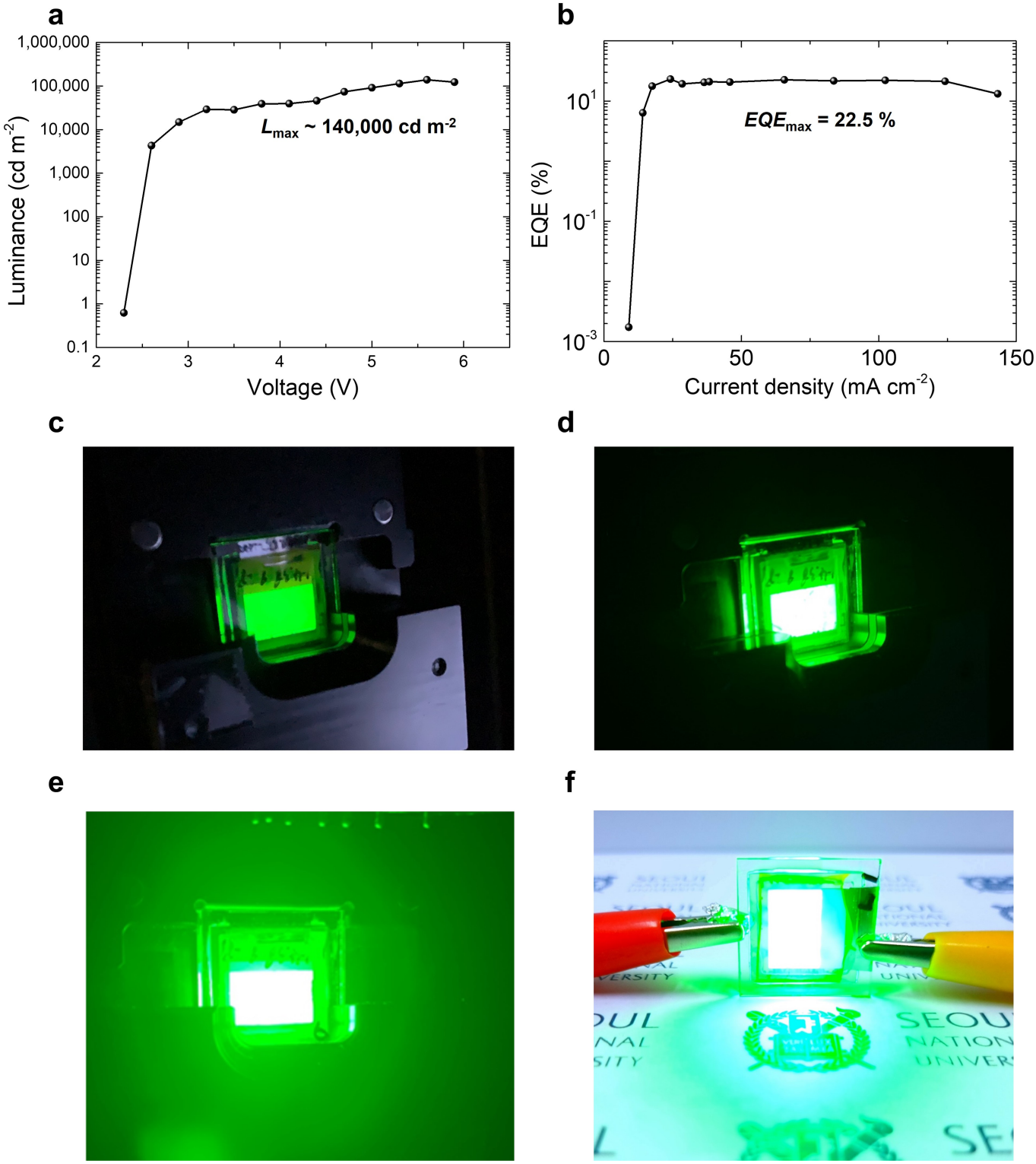

Extended Data Fig. 8 | Large-area devices. a, Luminance versus voltage; **b**, EQE versus current density of large-area devices based on in situ core/shell perovskites. **c**–**f**, Photographs of large-area devices (pixel size: 120 mm^2) operating at: **c**, < 10 cd m^{-2}; **d**, 1,000 cd m^{-2}; **e**, 100,000 cd m^{-2}; and **f**, 100,000 cd m^{-2} under daylight, showing uniform emission over the pixel.

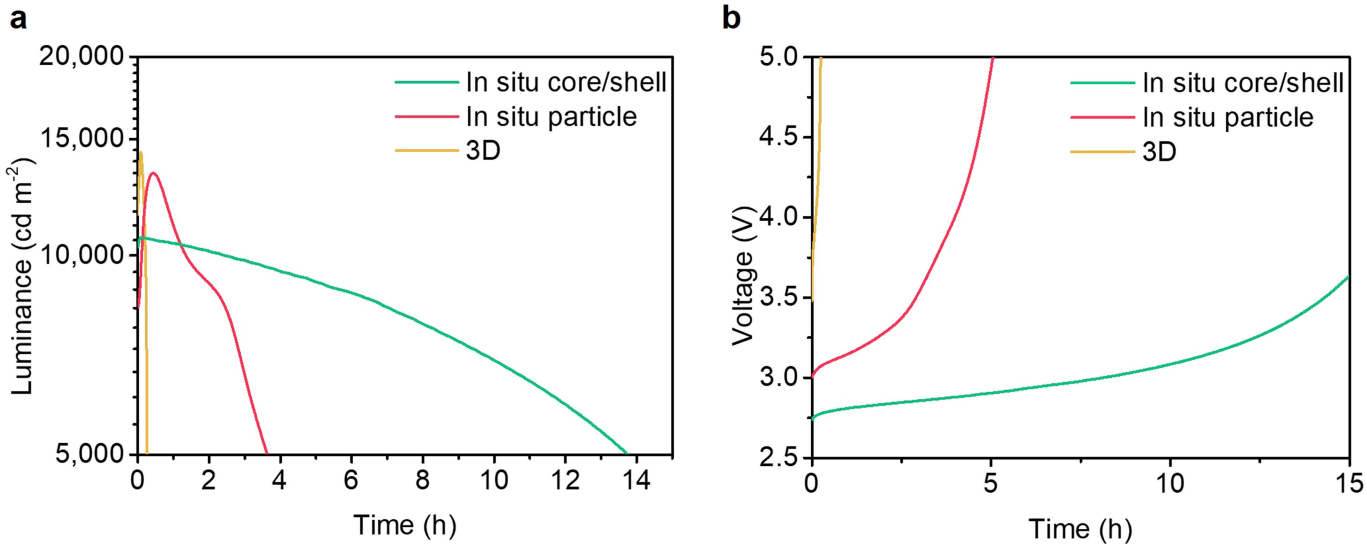

Extended Data Fig. 9 | Operational lifetime of PeLEDs. a, Luminance versus time of PeLEDs based on 3D, in situ particle, and in situ core/shell perovskites at initial brightness of 10,000 cd m^{-2}, and **b**, corresponding driving voltage versus operation time.

Extended Data Table 1 | Summarized electrical and luminance characteristics of PeLEDs

Perovskite	$V_{turn\text{-}on}$ at 1 cd m^{-2}	L_{max} (cd m^{-2}) (at bias (V))	EQE_{max} (%) (at bias (V))	CE_{max} (cd A^{-1}) (at bias (V))	PE_{max} (lm W^{-1}) (at bias (V))
3D	2.31	20,271 (4.1)	3.66 (3.2)	22.41 (3.2)	19.8 (3.2)
In situ particle	2.31	149,331 (5.0)	8.29 (4.1)	41.05 (4.4)	27.2 (4.1)
In situ core/shell	2.22	473,990(5.0)	28.9(4.1)	151.1(4.1)	112.8 (3.5)

$V_{turn\text{-}on}$: Voltage at luminance of 1 cd m^{-2}, L_{max}: maximum luminance, EQE_{max}: maximum EQE, CE_{max}: maximum current efficiency.